

## Reduction of wind stress due to swell at high wind conditions

H. García-Nava,<sup>1</sup> F. J. Ocampo-Torres,<sup>1</sup> P. A. Hwang,<sup>2</sup> and P. Osuna<sup>1</sup>

Received 16 December 2011; revised 13 March 2012; accepted 2 April 2012; published 19 May 2012.

[1] Wind stress over the ocean depends on the sea surface roughness which is determined by the sea state. On one hand, underdeveloped wind seas, rougher than their fully developed counterpart, increase the drag. On the other hand, the presence of swell can modify wind stress by modifying the wind sea roughness. This latter mechanism is believed to have a great impact at high winds whenever underdeveloped local waves coexist with swell. Detailed measurements of wind stress and wavefield in fetch-limited growth conditions were made in an area subjected to strong and persistent winds. Through the analysis of wavefield observations, it is found that the presence of swell dampens the short wind waves. The observed attenuation is greater for younger wind seas and decreases as the wind waves become older. Results obtained from modeling the interaction of wind waves and the air flow above point out that the attenuation of short wind waves causes a reduction of the wave-supported stress, which in turn decreases the total wind stress.

**Citation:** García-Nava, H., F. J. Ocampo-Torres, P. A. Hwang, and P. Osuna (2012), Reduction of wind stress due to swell at high wind conditions, *J. Geophys. Res.*, *117*, C00J11, doi:10.1029/2011JC007833.

### 1. Introduction

[2] The wind stress is a key parameter for ocean and atmosphere dynamics and coupling. The momentum exchange between the air flow and the sea is determinant in processes that occur at the upper ocean and lower atmosphere layers, in a broad time and spatial scales. The processes impacted range from mixing and wave generation to storm development and large scale ocean and atmosphere dynamics. Over the ocean, wind stress depends on the aerodynamic roughness of the sea surface,  $z_0$ , which is physically related to the waves. Thus, the sea state, among other parameters, modifies the momentum transfer between the ocean and the atmosphere.

[3] Wind wave development depends on the fetch and duration of driving wind. Theoretically, the waves may reach a fully developed state for unlimited fetch and unlimited duration. For a given wind speed, as fetch reduces waves become less developed or “younger”, as compared with the more developed “older” waves observed at a longer fetch. Young waves are rougher than their older counterpart and have been associated with increased stress [Donelan, 1990; Drennan *et al.*, 2003].

[4] The presence of swell modifies the wind stress in at least two ways: (1) swell can exchange momentum with the air flow [e.g., Grachev and Fairall, 2001; Kudryavtsev and

Makin, 2004], and (2) swell can modify the wind sea associated roughness [Donelan and Dobson, 2001]. The former modifies wind stress in low wind conditions where, depending on swell propagation direction relative to the wind, it enhances or reduces the drag [Donelan *et al.*, 1997; Drennan *et al.*, 1999]. The latter mechanism, far less studied, has been proposed to have an impact at higher winds in fetch-limited conditions where it is believed that swell causes a reduction of wind sea associated roughness [García-Nava *et al.*, 2009].

[5] Here we first explore the effect of swell on developing wind seas as observed through field measurements made on moderate to high wind conditions. Then, the impact of swell on wind stress is assessed by means of a comparison between the observed wind stress and that estimated through the quasi-linear theory of wind wave generation. The results suggest that the presence of swell dampens the short wind-waves, this reduces the amount of stress supported by the waves hence reducing the total wind stress in comparison with the corresponding wind stress in the absence of swell.

[6] This paper is organized as follows: In section 2 we briefly describe the field campaign and the procedures of numerical experiments. Results on the effect of swell on the wind sea and its impact on wind stress are presented in section 3. Further discussions and conclusions are drawn in section 4.

### 2. Experiment Description

#### 2.1. Field Measurements

[7] Field measurements were made during the Gulf of Tehuantepec air-sea interaction experiment (INTOA). The INTOA experiment took place from February to April 2005 in the Gulf of Tehuantepec as part of a program to study the physical and biological response of the Gulf of Tehuantepec coastal waters to the strong and persistent offshore wind that

<sup>1</sup>Departamento de Oceanografía Física, Centro de Investigación Científica y de Educación Superior de Ensenada CICESE, Ensenada, Mexico.

<sup>2</sup>Remote Sensing Division, Naval Research Laboratory, Washington, D. C., USA.

Corresponding author: H. García-Nava, Departamento de Oceanografía Física, Centro de Investigación Científica y de Educación Superior de Ensenada, Km. 107 Carretera Tijuana-Ensenada, Ensenada, BC 22860, Mexico. (hgarcia@cicese.mx)

occur in the region. In this context INTOA's goal was to study the air-sea interaction processes under this particular condition. In the following we give a brief description of the Gulf of Tehuantepec area, data collection and processing. A more comprehensive description of the INTOA experiment is given by *Ocampo-Torres et al.* [2011].

### 2.1.1. Gulf of Tehuantepec

[8] The Gulf of Tehuantepec is located in the Pacific Ocean at the southeast of México. This region is well known for the occurrence of the so-called *Tehuano* events, strong and persistent mountain gap winds that blow offshore with speeds that can exceed  $20 \text{ ms}^{-1}$ .

[9] The *Tehuano* events commonly occur during the winter [*Romero-Centeno et al.*, 2003]. A single event can last from a few hours to several days. In winter, swell arrives the area from the south; so during a *Tehuano* event swell propagates against the wind and the young locally generated wind sea coexists with the incoming swell.

### 2.1.2. Data Collection and Processing

[10] Wind and wave observations were made from a moored Air-Sea Interaction Spar (ASIS) buoy, deployed in the central part of the Gulf of Tehuantepec at  $16^\circ\text{N}$  and  $95^\circ\text{W}$  from February to April 2005. At this location the buoy was fixed at 22 km from the coast in a 60 m depth area.

[11] The ASIS buoy continuously sampled atmospheric turbulence, the wavefield and other related atmospheric and oceanic variables. The three dimensional wind velocity vector  $\mathbf{U} = (U, V, W)$  was measured with a sonic anemometer at 6.5 m above the sea level. Surface elevation was measured with an array of 8 wave wires. Wind speed and surface elevations were corrected for buoy motion following algorithms described by *Anctil et al.* [1994] and *Drennan et al.* [1994].

[12] Wind speed was decomposed in its mean,  $\bar{U}$ , and turbulent,  $\mathbf{u}'$ , components as  $\mathbf{U} = \bar{U} + \mathbf{u}'$ . Wind stress was computed from the turbulent components through the covariance method

$$\boldsymbol{\tau} = \rho_a \overline{(\mathbf{u}'w', v'w')} \quad (1)$$

where  $\rho_a$  is the air density and the over bars denote a temporal mean over a 30 min period.

[13] Wave parameters were obtained from the motion-corrected surface elevation measurements. Wave variance was computed as the integral of the frequency spectrum and the variance of wind sea and swell were computed as the integral over the corresponding frequencies. Throughout this paper we use the wave variance to represent the wave energy,  $E$ . The wind sea and swell components of the wave spectrum were separated as described by *García-Nava et al.* [2009]. For the runs within the first 8 days, when reliable information from at least four wave staffs was available, the frequency and wave number directional spectra were calculated through the Maximum Likelihood Method (as described by *Drennan et al.* [1994]) and the Wavelet Directional Method [*Donelan et al.*, 1996], respectively.

[14] A full description of data acquisition and processing, as well as motion correction procedure and its induced error on wind stress calculation is given by *García-Nava et al.* [2009].

[15] From the whole data set we selected runs representative of fetch-limited wave growth at moderate to high wind conditions. In practice, we selected runs with wind speeds greater than  $7.5 \text{ ms}^{-1}$  and wind direction around  $180^\circ \pm 30^\circ$ .

These criteria ensures that wind blows offshore and that the fetch, determined by the ASIS position, is shorter than that needed for the waves to reach its full development. In fact for  $U_{10} > 7.5 \text{ ms}^{-1}$  the wave age of the locally generated wind waves, defined as  $c_p/u_*$  where  $c_p$  is the phase speed of the spectral peak component, comply with  $c_p/u_* < 20$  considered as threshold for underdeveloped waves.

## 2.2. Quasi-Linear Theory

[16] The quasi-linear theory of wind wave generation, first introduced by *Fabrikant* [1976], describes the interaction of wind-generated gravity waves and the air flow above based on the Miles resonance mechanism. Here we use the approximation to the quasi-linear theory due to *Janssen* [1991]. The theory and its approximation is fully described in a series of papers by Peter Janssen and others [*Janssen et al.*, 1989; *Janssen*, 1991, 2004], therefore only a concise description follows.

[17] From conservation of momentum in steady conditions, the total air-water momentum flux is given by the sum of the turbulent stress  $\tau_{turb}$ , the viscous stress  $\tau_{visc}$ , and the wave-induced stress  $\tau_w$ , that is

$$\boldsymbol{\tau} = \tau_{turb} + \tau_{visc} + \tau_w. \quad (2)$$

Here, for convenience, the  $x$  axis points in the wind speed direction. The turbulent stress is modeled by means of a mixing length hypothesis

$$\tau_{turb} = \rho_a l^2 \left| \frac{\partial}{\partial z} U_0 \right| \frac{\partial}{\partial z} U_0, \quad (3)$$

where  $l = \kappa z$  is the mixing length,  $z$  is the vertical coordinate with the mean surface at  $z = 0$ ,  $U_0(z)$  is the wind profile, and  $\kappa$  is the von Kármán constant. The viscous stress is given by

$$\tau_{visc} = \mu_a \frac{\partial}{\partial z} U_0, \quad (4)$$

with  $\mu_a$ , as the dynamic viscosity of air.

[18] Wave-induced stress represents a loss of momentum from the air flow. At the surface this momentum loss can be related to the rate of change of wave momentum  $M$  due to wind, as

$$\tau_w(z=0) = \int \frac{\partial}{\partial t} M \Big|_{wind} dk d\theta, \quad (5)$$

for linear waves the wave momentum is given by the expression

$$M = \rho_w g k \omega^{-1} \Phi(k, \theta) \hat{l}, \quad (6)$$

where  $\rho_w$  is the water density,  $g$  is the gravitational acceleration,  $\omega$  is the wave angular frequency,  $\Phi(k, \theta)$  is the wave number spectrum, and  $\hat{l}$  is the unit vector in the wave number direction [*Janssen*, 1989, 2004].

[19] The change in wave momentum exerted by the wind must be compensated by the growth of wind waves  $S_{in}$ , that can be estimated from the wave growth rate  $\gamma$  as follows

$$\frac{\partial}{\partial t} \Phi \Big|_{wind} = S_{in} = \gamma \Phi(k, \theta). \quad (7)$$

The corresponding wave growth rate can be written as

$$\gamma = \epsilon \beta \omega \left( \frac{u_*}{c} \right)^2 \cos^2 \theta, \quad (8)$$

where  $u_* = \sqrt{\tau/\rho_a}$  is the friction velocity,  $\epsilon$  is the air-water density ratio,  $c$  is the wave phase speed,  $\theta$  is the waves propagation direction, and  $\beta$  is the so-called Miles parameter. According to *Janssen* [1991]  $\beta$  can be parameterized as

$$\beta = \frac{1.2}{\kappa^2} \xi \ln^4 \xi, \quad (9)$$

where  $\xi$  is the critical height defined as

$$\xi = \left( \frac{u_*}{\kappa C} \right)^2 \Omega e^{\kappa c/u_* \cos \theta}, \quad |\theta| \leq \frac{\pi}{2}, \quad (10)$$

$\Omega$  is the profile parameter

$$\Omega = \frac{gz_2 \kappa^2}{u_*^2}, \quad (11)$$

and  $z_2 = z_0 + z_1$  is the surface roughness, expressed in this way to distinguish between the effects of gravity-capillary waves and gravity waves. The effect of gravity-capillary waves is modeled by means of the Charnock relation  $z_0 = \alpha u_*^2/g$ , with  $\alpha = \text{constant}$ , and the effect of short gravity waves is introduced to the model by means of  $z_1$ , which is solved as part of the problem. Then, the logarithmic wind profile that satisfies  $U_0(z_0) = 0$  is

$$U_0(z) = \frac{u_*}{\kappa} \ln \left( \frac{z + z_1}{z_0 + z_1} \right). \quad (12)$$

[20] At a height  $z = z_0$  the effect of viscous stress can be neglected, the momentum balance becomes  $\tau = \tau_{turb}(z_0) + \tau_w(z_0)$ , and an expression for  $z_1$  can be found if  $\tau_{turb}(z = z_0)$  is evaluated from (3) using (12), such as

$$z_1 = z_0 \left( \frac{1}{\sqrt{1 - \tau_w/\tau}} - 1 \right). \quad (13)$$

From the wind profile (equation (12)) at a height  $z \gg z_1$  we can get an expression for the total stress as

$$\tau = \rho_a \left[ \frac{\kappa U_0(z)}{\ln(z/z_2)} \right]^2. \quad (14)$$

[21] Now, with wave growth rate expression (8), wave induced stress can be written in terms of wave directional frequency spectrum  $F(f, \theta)$  as

$$\tau_w = \tau \int_0^\infty \int_{-\pi/2}^{\pi/2} k^2 \beta F(f, \theta) \cos^2 \theta \hat{d}\theta df, \quad (15)$$

where we have used the deep water dispersion relationship  $\omega^2 = gk$ .

[22] Thus, for any given wind speed and directional frequency spectrum, wind stress can be calculated by solving (14) and (15) iteratively.

### 2.2.1. Wave Frequency Spectrum Approximation

[23] To estimate the stress from a non-directional wave spectrum, i.e. frequency spectrum  $E(f)$ , we must assume

that  $\beta$  is independent of the wave propagation direction, which will be a reasonable assumption for waves traveling close to the wind direction as is the case for small and strongly forced waves. Wave directional spectrum can be expressed as the product of the frequency spectrum and a directional spreading function  $D(f, \theta)$  such as

$$F(f, \theta) = E(f)D(f, \theta), \quad (16)$$

where the spreading function must satisfy  $\int_{-\pi}^{\pi} D(f, \theta) d\theta = 1$  in order to preserve the wave energy. With these last assumptions (15) can be rewritten as

$$\begin{aligned} \tau_w &\simeq \tau \int_0^\infty k^2 \beta E(f) \int_{-\pi/2}^{\pi/2} D(f, \theta) \cos^2 \theta \hat{d}\theta df \\ \tau_w &= \mathcal{C} \tau \int_0^\infty k^2 \beta E(f) df, \end{aligned} \quad (17)$$

where  $\mathcal{C}$  is the result of the evaluation of the integral over direction. Then, total stress can now be computed from the wind speed and the wave frequency spectrum using (14) and (17).

[24] Most commonly used directional spreading function has the form of cosine to the  $2s$  power [*Longuet-Higgins et al.*, 1963], such as

$$D_{\cos} = \mathcal{N}(s) \cos^{2s}(0.5(\theta - \hat{\theta})) \quad (18)$$

where  $s$  is a function of the dimensionless frequency  $f/f_p$  and the inverse wave age  $U/c_p$ ,  $U$  is the wind speed, and  $\mathcal{N}(s)$  is a constant. The Gulf of Tehuatepec data used here are characterized by  $1.5 < U/c_p < 2.6$ . For this range of  $U/c_p$  the mean values of  $\mathcal{C}$  are in the range  $0.46 < \mathcal{C} < 0.55$ . Here we used  $\mathcal{C} = 0.5$ .

[25] To test this approximation,  $u_*$  was estimated through quasi-linear theory with both the frequency and directional wave spectra for the period when directional wave information is available. There is a very good agreement between both estimates, the mean difference between estimates is 4% with a standard deviation of 2%. Almost all the computed differences (95%) are lower than 7% and never exceed 10%.

[26] By setting  $\mathcal{C}$  as a constant we have imposed a constrain on the shape of the spreading function. However, we can further assume that the angular spreading of the wave energy is the same at all frequencies. This is a widely used assumption for waves few times shorter than the peak wavelength [*Donelan et al.*, 1985], which support a great part of the surface stress.

[27] Finally, it is important to notice that although the wave directional distribution (18) is sufficient for our purpose of setting a value for  $\mathcal{C}$ , it does not represent adequately some directional features observed recently, as the bimodal structure of angular distribution observed at high frequencies [*Long and Resio*, 2007; *Romero and Melville*, 2010].

### 2.3. Wave Coupled Model

[28] In this study we use the WAM wave model to provide an independent estimate of the wind stress for offshore winds in the absences of swell. The procedure that the WAM wave model [*WAMDI*, 1988; *Komen et al.*, 1996] uses to estimates wind stress is outlined below.

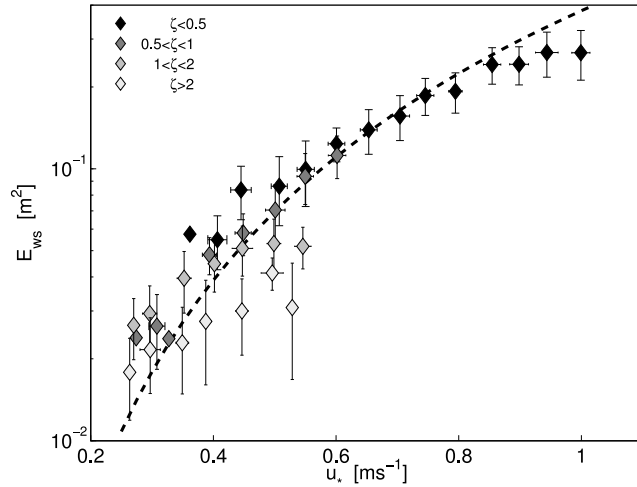


**Figure 1.** Wind-sea energy  $E_w$  as function of friction velocity  $u_*$ . The diamonds are the mean value for bins of scaling velocity at different swell index  $\zeta$  ranges (gray scale) and the dashed line is the best fit to the BHDDB data ensemble.

[29] The model describes the evolution of the directional spectrum by solving the wave energy balance equation

$$\frac{\partial F}{\partial t} + \nabla_x(C_g F) + \nabla_{f,\theta}(C_g F) = S(f, \theta) = S_{in} + S_{nl} + S_{ds}, \quad (19)$$

where  $S$ , the source term, represents the gain or loss of wave energy through independent physical processes: wave growth by wind  $S_{in}$ , wave-wave nonlinear interactions  $S_{nl}$ , and dissipation by whitecapping  $S_{ds}$ .

[30] In the current standard version of the WAM model (Cycle 4.5), waves are coupled to the atmospheric surface layer via the quasi-linear theory,  $S_{in}$  is computed from (7), and  $u_*$  estimated by solving (14) and (15).

[31] Since the conditions we wanted to reproduce correspond to winds blowing offshore nearly perpendicular to the coast, we performed a series of numerical experiments with a one dimensional version of the WAM model. The numerical domain was 30 km long with a constant depth of 60 m and the coast at one end. The wind was kept constant within 6 days for each model run. Output data used here correspond to the last simulated time for a node at 22 km from the coast, approximately the same position of the ASIS buoy during the INTOA experiment. Wind speed was varied from  $8 \text{ ms}^{-1}$  to  $20 \text{ ms}^{-1}$ .

### 3. Analysis of Results

#### 3.1. Swell Influence on the Wind Waves

[32] In Figure 1 we show the wind sea energy  $E_w$  as a function of friction velocity, as observed during the INTOA experiment. The gray scale represents the relative importance of swell through the swell index  $\zeta$ , defined as the energy of swell  $E_s$  divided by the wind sea energy, such as

$$\zeta = \frac{E_s}{E_w}, \quad (20)$$

so the relative importance of swell increases as  $\zeta$  increases. The results presented in Figure 1 clearly show a decreasing wind sea energy as the swell index increases despite of the large statistical variability. These results point out that the long period swell present during INTOA dampens the short wind generated waves. In this figure, the dashed line represent the empirical wave growth function for mixed seas obtained from the BHDDB data ensemble [Hwang *et al.*, 2011b]. The BHDDB data ensemble is a compilation of five individual data sets obtained in near-neutral atmospheric stability and steady wind conditions [Burling, 1959; Hasselmann *et al.*, 1973; Donelan *et al.*, 1985; Dobson *et al.*, 1989; Babanin and Soloviev, 1998] used to represent the fetch-limited wave growth in “ideal” conditions [e.g., Hwang and Wang, 2004b; Hwang *et al.*, 2011b].

[33] Now, we will explore the effect of swell on the short wind waves by means of an analysis of the spectral equilibrium range and the dimensionless wave number spectrum,  $B(k) = \phi(k)k^3$ , the so-called saturation spectrum. In this section we specially consider the wave number spectra rather than the frequency spectra since the latter can be distorted by Doppler-shifting particularly at high frequencies.

[34] Characteristically, wind-wave spectra exhibit a region in the immediate vicinity of the peak toward higher frequencies, where the wave energy is in dynamic balance. Within this region, known as the equilibrium range, it is now generally accepted that the spectral shape is given by

$$\phi(k)_{eq} = bu_*g^{-0.5}k^{-2.5}, \quad (21)$$

where  $g$  is the gravitational acceleration and  $b$  is a dimensionless coefficient. Early wave studies suggested  $b$  as a constant [see, e.g., Phillips, 1985, Table 1], and more recent studies have found that  $b$  depends on wave age  $c_p/u_*$  [Resio *et al.*, 2004; Long and Resio, 2007; Romero and Melville, 2010]. In any case, for a given spectrum the quantity  $\varepsilon = \phi(k)k^{2.5}$  is expected to remain relatively constant within the equilibrium range so in this sense  $\varepsilon$  gives an idea of the energy level of the short waves.

[35] The observed  $\phi(k)$  presents an equilibrium range around  $2.25 < k/k_p < 9.0$ , which correspond to frequencies in the range  $1.5 < f/f_p < 3.0$ . Within this frequency range  $\varepsilon$  was computed as  $\varepsilon = \langle \phi(k)k^{5/2} \rangle_{eq}$ , where the brackets denote the average over this particular range.

[36] Figure 2 shows  $\varepsilon$  as a function of a scaling velocity proposed by Resio *et al.* [2004], such as  $u_a = u_*(c_p/u_*)^{1/3}$  and characterized with the swell index,  $\zeta$ . Although there is some resemblance of a linear trend with  $u_a$ ,  $\varepsilon$  values are somewhat scattered. The observed  $\varepsilon$  tends to be lower than that observed by Resio *et al.* [2004] in the absence of swell (Dash dotted line) and it decreases as the swell becomes more important. In this figure, the dashed line represents the GoTEX (acronym of Gulf of Tehuantepec Experiment) results [Romero and Melville, 2010], as can be seen these results are in better agreement with the INTOA data, specially when the wind sea energy exceeds the corresponding swell energy (solid line). The GoTEX measurements were made at the Gulf of Tehuantepec in similar wind conditions as the INTOA experiment. The GoTEX wave spectra given by Romero and Melville [2010, Figure 8] show a ubiquitous presence of swell and suggest that GoTEX measurements correspond to wind sea dominated conditions. Also notice

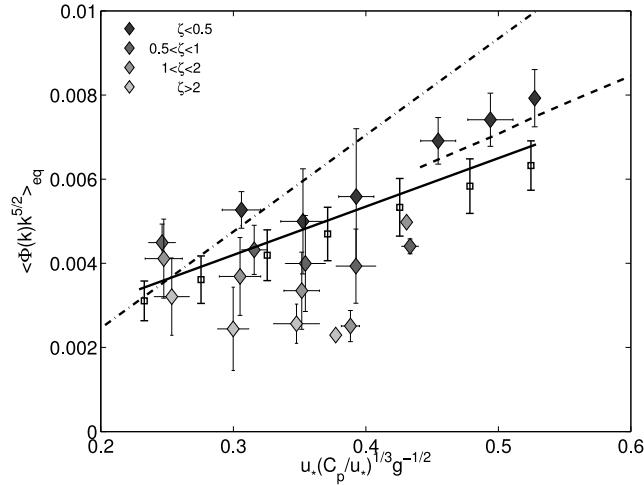


**Figure 2.** Characteristic energy level of short waves  $\varepsilon = \langle \phi(k)k^{5/2} \rangle_{eq}$  as a function of scaling velocity  $(u_*^2 c_p)^{1/3}$ . The diamonds are the mean value for bins of scaling velocity at different swell index  $\zeta$  ranges (gray scale). The open squares are bin-averaged estimates obtained using the equilibrium range parameterization by Romero and Melville [2010] and this study's measurements of  $u_*$  and  $c_p$ . The error bars are two standard deviations. Lines represent the linear fit to observed data with  $\zeta < 1$  (solid) and the data fits by Resio et al. [2004] (dash-dotted) and Romero and Melville [2010] (dashed).

that Hwang et al. [2011b] find out an underestimation between 10% and 15% on the determination of  $u_*$  during GoTEX and so, the GoTEX data shown in Figure 2 were corrected assuming a constant 10% underestimation on  $u_*$ .

[37] Similarly to the determination of  $\varepsilon$  performed here, both Resio et al. [2004] and Romero and Melville [2010] computed  $\varepsilon$  within the range  $1.5 < f/f_p < 3.0$ . Although, Resio et al. [2004] used  $2.5f_p$  as the lower limit for two of the data sets in their analysis to avoid shoaling wave harmonics.

[38] It is known that atmospheric stability can affect the wave growth rate [e.g., Kahma and Calhoun, 1996]. Data presented here were collected under neutral and weakly stable conditions represented by  $-0.01 < z/L < 0.1$ , where  $L$  is the Obukhov length. No correlation between  $\varepsilon$  and the stability parameter  $z/L$  was noted. These findings agree well with those of Romero and Melville [2010] who also offer a more comprehensive discussion on the subject.

[39] The results presented in Figure 2 suggest that the swell may cause a reduction of the energy of the short waves. Following up with another approach of analysis, from the deep water wave dispersion relation  $\omega^2 = gk$ , the spectral form of the equilibrium range (21) can be written as

$$\phi(k)_{eq} = b \left( \frac{u_*}{c} \right) k^{-3}, \quad (22)$$

and the saturation spectrum can be expressed as

$$B(k)_{eq} = b \left( \frac{u_*}{c} \right). \quad (23)$$

In general, for waves several times shorter than the dominant waves, the dependence of  $B(k)$  on wave age can be

expressed by a power law function [Hwang and Wang, 2004a], such as

$$B \left( k; \frac{u_*}{c} \right) = A_0(k) \left( \frac{u_*}{c} \right)^{a_0(k)}. \quad (24)$$

where  $A_0$  is a shape factor of the dimensionless spectrum and  $a_0$  is the exponent of the spectral dependence on wind-forcing [Hwang, 2008].

[40] The swell index ( $\zeta$ ) not only gives an idea of the swell energy, but also expresses the relevance of the wind-forcing through the energy level of the wind sea. Therefore, a range of  $\zeta$  where it is randomly distributed as a function of  $u_*$  is required to ensure that different bins of  $\zeta$  will have a similar dependence on wind stress for the analysis to capture changes due to swell. For the selected range of the swell index ( $0 < \zeta < 1.52$ ), four bins named from B1 to B4 were defined (Table 1). Within each  $\zeta$  bin  $A_0$  and  $a_0$  were computed using least squares fitting of the saturation spectra as a function of the inverse wave age. B1 includes cases with the energy of wind sea is at least four times higher than swell energy, B2 and B3 include cases of decreasing wind sea dominance, and B4 only cases of swell dominated conditions. All bins have a similar wind speed range, with the exception of B1 which include higher wind speeds. B1 was kept for the analysis because it represents the least swell-influenced conditions and nearly matches the definition of the least swell-influenced conditions of Hwang [2008].

[41] The computed values of  $A_0$  and  $a_0$  progressively decrease as  $\zeta$  increases (Figure 3). Both  $A_0$  and  $a_0$  computed for B1 (circles) are in good agreement with those reported by Hwang [2008] for  $\zeta < 0.2$  (solid line).

[42] Figure 4 shows examples of the saturation spectra, computed from (24) using the calculated values of  $A_0$  and  $a_0$ , for different values of  $u_*$ . The damping of the high frequency wind waves by swell can be seen in the progressive decrease of  $B(k)$  as  $\zeta$  increases. Somewhat surprisingly, the attenuation of short wind waves increases as the wind-forcing increases. The same conclusion can be drawn from results presented in Figure 2 where it can be seen that the differences between the reference  $\varepsilon$  in the absence of swell (dash-dotted line) and the computed values of  $\varepsilon$  for INTOA data (diamonds) seems to increase with the wind-forcing characterized by the scaling velocity.

[43] The INTOA data used within this work correspond to offshore winds blowing over a fixed fetch, determined by the distance between the coast and the ASIS buoy (see section 2). For these conditions as the wind-forcing increases waves become younger, therefore the results shown in Figure 4 can be interpreted as greater damping of the short wind waves by swell for younger waves than for the older

**Table 1.** Characteristics of the Swell Index Bins Used for Dimensionless Wave Number Spectrum Analysis<sup>a</sup>

Bin Id.	$\zeta$	$U_{10}$ (ms <sup>-1</sup> )	$z/L \times 10^{-2}$	No. Data
B1	0–0.26	14–17	0.44–1.12	14
B2	0.26–0.68	9–15	0.74–8.12	56
B3	0.68–1.10	7–14	–1.41–9.14	41
B4	1.10–1.52	7–14	–1.62–10.91	42

<sup>a</sup>For each bin named B1 to B4, ranges for swell index  $\zeta$ , wind speed  $U_{10}$ , and stability  $z/L$  are given. Number of data per bin is also shown.

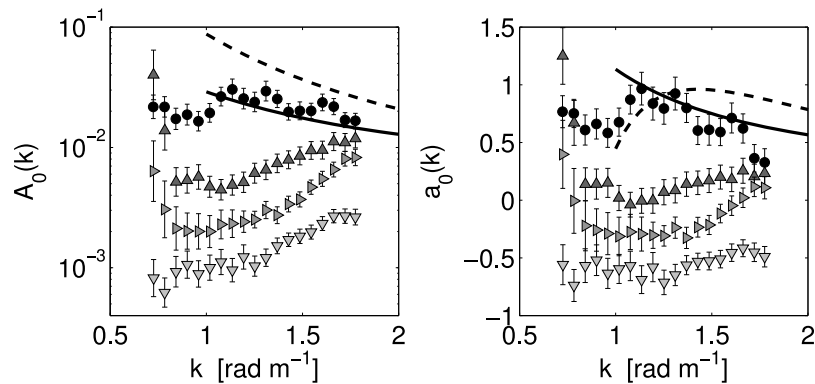


**Figure 3.** Coefficient  $A_0(k)$  and exponent  $a_0(k)$  of equation (24) as a function of the wave number, for the swell index ranges described in Table 1: B1 (circles), B2 (up triangles), B3 (right triangles), and B4 (down triangles). The error bars are the 95% confidence limits for the regression analysis. The solid and dashed lines represent the less and most influenced by swell conditions reported by *Hwang* [2008], respectively.

ones. Moreover, the presence of swell can cause an increase, rather than damping, of spectral energy for waves near full development (Figure 4, top left). These last results agree with those of *Hwang* [2008] who reported an increase of the spectral density with increasing swell index for the waves in the range  $1 \text{ m}^{-1} < k < 3 \text{ m}^{-1}$  for fully developed waves under light to moderate winds.

### 3.2. Effect of Wind Sea Damping on Wind Stress

[44] In the preceding section we determined that the swell dampens the wind sea. Here we investigate the impact of this

damping on wind stress by means of a comparison of the friction velocity observed during the INTOA experiment and that estimated through the quasi-linear theory.

[45] The wave number spectra could only be computed for a limited period of time at the beginning of the INTOA experiment (see explanation in section 2.1.2). For this period the observed conditions are largely confined to winds lower than  $12 \text{ ms}^{-1}$ . The results introduced in the preceding section suggest that the effect of swell on wind seas increases with increasing wind-forcing, therefore we would like to extend our analysis to the whole INTOA experiment measuring

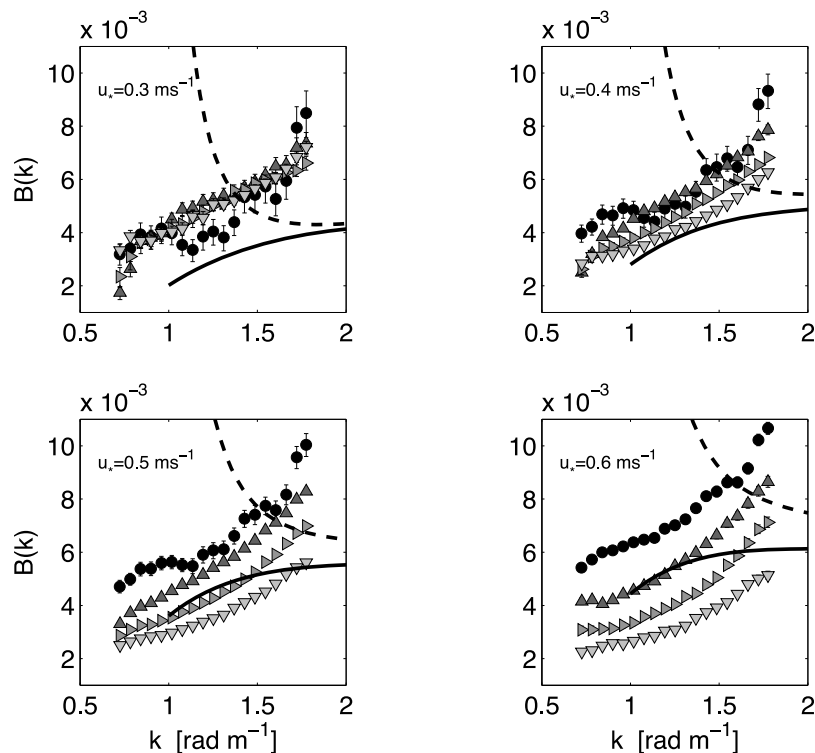


**Figure 4.** Saturation spectrum  $B(k)$  computed through equation (24) with the calculated values of  $A_0$  and  $a_0$ , for different values of the friction velocity. The symbols denote the swell index ranges described in Table 1: B1 (circles), B2 (up triangles), B3 (right triangles), and B4 (down triangles). The solid and dashed lines represent the less and most influenced by swell conditions reported by *Hwang* [2008], respectively.

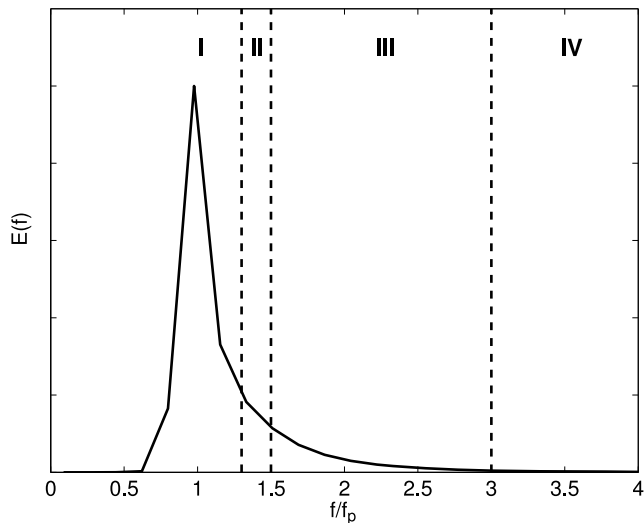


**Figure 5.** Diagram of a wave frequency spectrum showing its different regions: I peak region, II transitions region, III equilibrium range, and IV dissipation range.

period. In order to do so, we need to use the wave frequency spectra to compute  $u_*$  with the quasi-linear theory. However, it is well known that temporal point measurements, as the ones used here to compute the wave frequency spectra, are affected by the Doppler-shifting caused by surface currents on the whole spectrum and by the orbital motions of the longer waves on the shorter ones. As a consequence of Doppler-shifting, energy levels at high frequencies are increased and spectral slope is reduced [Banner, 1990]. Short waves are apparently steeper than what they actually are, artificially increasing the amount of momentum they can support and hence estimates of  $u_*$  from quasi-linear theory will be artificially increased.

[46] So, before  $u_*$  was computed from frequency spectra through the quasi-linear theory, we first reconstructed the observed wave frequency spectra to alleviate Doppler-shifting at the high frequency tail of the spectrum. Wave frequency spectra are reconstructed as follow: Each frequency spectrum was divided into four regions: the peak region, a transition region, the equilibrium range, and the dissipation range (Figure 5). Within the peak region we assume that the Doppler effects are negligible and so the energy of observed  $E(f)$  is kept unchanged. In our observations the equilibrium range is readily apparent and therefore set to  $1.5 < f/f_p < 3$ . In this range wave energy was computed from the equilibrium range parameterization of Romero and Melville [2010] (squares in Figure 2). In accordance with our previous results, the use of this parameterization will include in some degree the attenuation of the high frequency waves by swell. A smooth transition between the peak region and the equilibrium range was ensured by means of running average within the transition region. Finally, a spectral tail proportional to  $f^{-5}$  was imposed at the dissipation range. Figure 6 shows examples of reconstructed spectra for different wave ages.

[47] Figure 7 shows that the quasi-linear theory simulates quite well the  $u_*$  observed during the INTOA experiment when  $u_*$  is computed using the measured wave number and frequency spectra (dark and light circles, respectively). In contrast, the observed  $u_*$  is overestimated by the  $u_*$

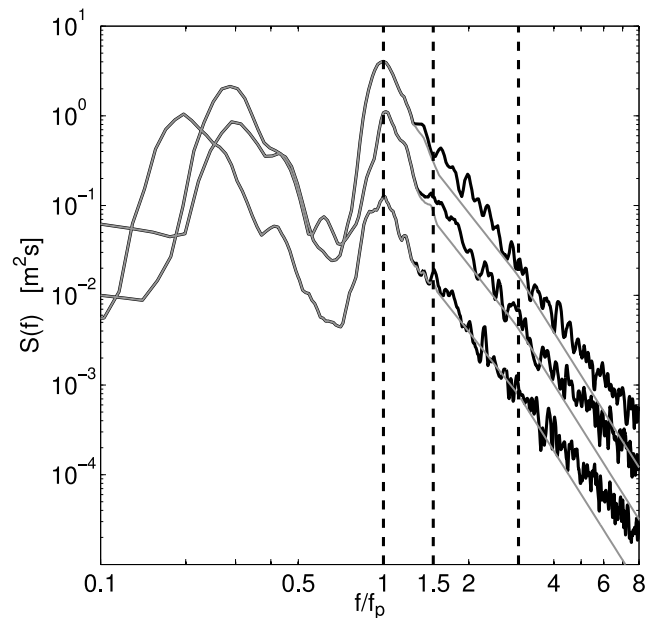


**Figure 6.** Examples of reconstructed spectra for different wave ages. From top to bottom  $c_p/u_* = 8.2, 13,$  and  $18,$  respectively. Lines represent the observed (black) and reconstructed (gray) wave spectra.

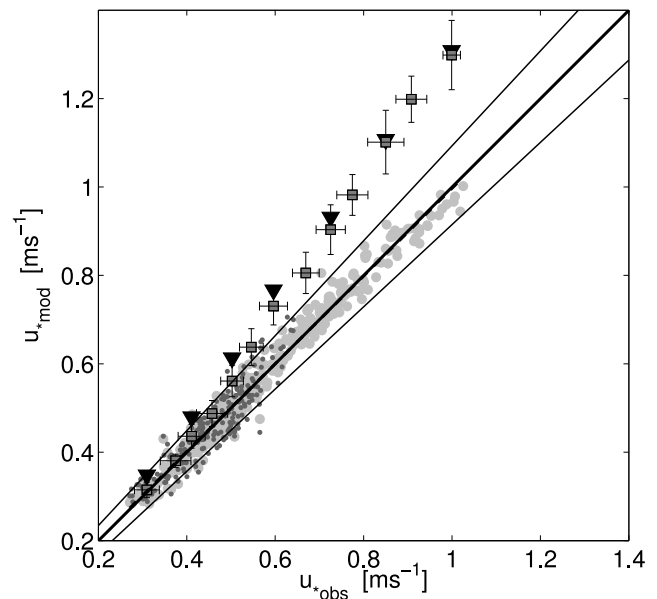


**Figure 7.** Comparison of observed friction velocity and the friction velocity modeled with quasi-linear theory using the observed wave number spectra (dark dots) and the reconstructed wave number spectra with Romero and Melville [2010] equilibrium range parameterization (light dots). Also shown is the friction velocity expected for pure wind seas as computed with the WAM model (down triangles) and through the roughness parameterization proposed by Drennan et al. [2003] (squares). Lines represent the 1:1 relationship (thick-solid), the linear fit (dashed), and the 90% confidence intervals based on the sampling variability of the INTOA data (thin-solid).

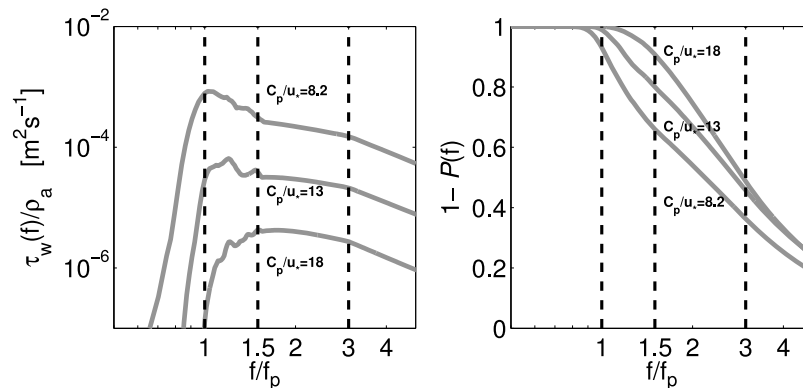


**Figure 8.** The (left) wave stress spectrum and (right) waves stress fraction as a function of dimensionless frequency, for the spectra shown in Figure 6.

computed through the WAM model (triangles) and with our measurements of  $c_p$  together with the drag coefficient function for pure wind seas proposed by *Drennan et al.* [2003] (squares). Both estimations, from the WAM model and from *Drennan et al.* [2003] relationship, are in good agreement with each other and they represent a reference  $u_*$  as expected in the absence of swell. The difference between the observed  $u_*$  and that computed in the absence of swell (squares and triangles) increases with wind speed (wind speed increases up and right in Figure 7). For the INTOA data used here (fetch-limited wind seas), wind waves become younger with increasing wind speed and so, larger differences in  $u_*$  between observations and the references in the absence of swell occur for less developed wind seas for which the attenuation of short wind waves by swell is more important (see section 3.1). These results show that the attenuation of wind sea by swell causes a reduction of the wind stress as compared with the corresponding stress in the absence of swell and that this reductions increases as wind sea becomes younger.

[48] In developing seas most of the drag is determined by the wave induced stress [*Janssen, 1991*] from which a large part is supported by the short waves [*Makin and Kudryavtsev, 1999*]. If we define the cumulative sum of the normalized wave stress  $P(f)$  as

$$P(f) = \frac{1}{\tau_w} \int_{f_0}^f \tau_w(f') df', \quad (25)$$

where  $f_0$  is the lowest frequency, and  $\tau_w = \int \tau_w(f) df$  is the total wave stress. Then, the quantity  $(1 - P(f))$ , the cumulative wave stress, represents the fraction of the wave stress supported by waves with frequencies equal to or greater than a frequency  $f$ . The left and right panels of Figure 8 show, respectively, the wave stress spectrum computed according to (17) and the waves stress fraction for the spectra shown in Figure 6. For waves near full development, such as  $c_p/u_* = 18$ , almost all wave stress is supported by waves within the equilibrium and dissipation ranges ( $f > 1.5f_p$ ). As waves become less developed, although short waves still support a large part of the wave stress, the momentum transfer to the peak region greatly increases. At the less developed conditions presented in Figure 8 short waves support more than 60% of the total wave stress.

[49] The effect of swell on the high frequency tail of the spectra will not be accounted if we use the equilibrium range parameterization of *Resio et al.* [2004] (dash-dotted line in Figure 2) for the frequency spectra reconstruction. In accordance to our previous results, with this reconstruction we can estimate  $u_*$  through quasi-linear theory, resembling pure wind sea conditions. Figure 9 (left) shows a comparison of such  $u_*$  estimates and the ones observed during the INTOA experiment. As it can be seen, these values are greatly overestimated in comparison to the observations but they present a close agreement with  $u_*$  computed for pure wind seas through the WAM model (triangles) and the parameterization proposed by *Drennan et al.* [2003] (squares).

[50] It is expected that the attenuation of wind waves caused by swell occurs within the whole wind sea spectrum. In the results shown in Figure 9 (left), the effect of swell was removed only from the high frequency tail of the spectra. For wind seas near full development almost all of the wave stress is supported by these short waves, while for less developed wind seas the waves within the peak region support about 40% of the wave stress (Figure 8). So, the results from the quasi-linear theory for pure wind seas are underestimated for the less developed wind seas (upper right corner of Figure 9 (left)). Now, if we assume that the energy contained in the peak region of the observed spectra is attenuated by some 1% and increase the spectral energy within this region by this amount, the estimates of  $u_*$  from quasi-linear theory agree better with those expected for pure wind-seas as computed through the WAM model and the relationship proposed by *Drennan et al.* [2003] (Figure 9, right).

#### 4. Discussion and Conclusions

[51] The analysis of the wave measurements made during the INTOA experiment show that the presence of swell dampens the wind waves. The observations of high frequency waves are in good agreement with the recent observations of *Romero and Melville* [2010], carried out in the same area under similar conditions. From the analysis of the dimensionless wave spectrum we found that the attenuation of short wind waves, caused by swell, depends on wave age: the attenuation is greater for younger wind seas (higher wind-forcing) and decreases for older wind seas (lower forcing). Furthermore, the presence of swell can cause an

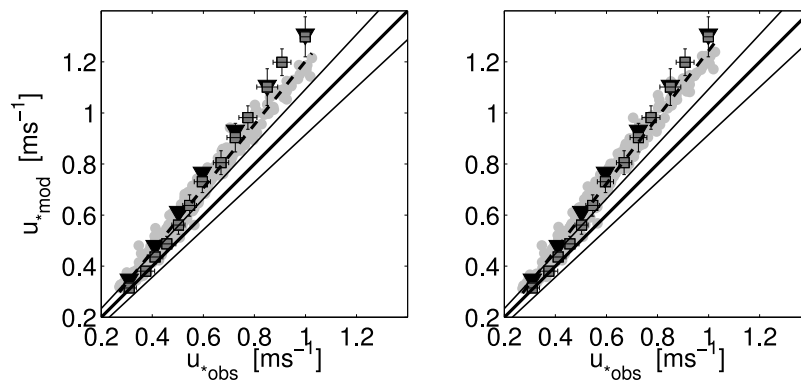


**Figure 9.** As in Figure 7 but for the reconstructed  $E(f)$  using the equilibrium range parameterization proposed by Resio *et al.* [2004] (light dots in the left panel) and the reconstructed  $E(f)$  using the using the equilibrium range parameterization proposed by Resio *et al.* [2004] and assuming an attenuation of 1% at the energy within the spectral peak region (light dots in the right panel). Lines represent the 1:1 relationship (thick-solid), the linear fit (dashed), and the 90% confidence intervals based on the sampling variability of the INTOA data (thin-solid).

increase of the energy of the short wind waves, rather than damping, for fully developed waves under low wind conditions [Hwang, 2008].

[52] In developing wind seas most of the stress is determined by momentum transfer from wind to waves [Janssen, 1991] and a large part of the momentum flux is supported by the short waves [Makin and Kudryavtsev, 1999]. Hence, the attenuation of short wind waves by swell entails a reduction of the wind stress. In the framework of the quasi-linear theory of wind wave generation, the attenuation of the short waves reduces the wave stress, which lowers the surface aerodynamic roughness, so that the airflow is accelerated near the surface and the wind shear diminishes further reducing the shearing stress. However, the effect of wind sea damping is not as straight forward since both the turbulent and the wave induced stresses also depend on the total wind stress.

[53] Swell propagating against the wind has been associated with increased stress at low wind conditions [Donelan *et al.*, 1997]. Under these conditions the contribution of swell to the stress compensates for any reduction caused by the attenuation of wind sea [Donelan and Dobson, 2001]. However, the significance of the direct contribution of swell to drag decreases dramatically with increasing wind speed [Pan *et al.*, 2005], so at high winds the largest effect will be due to the attenuation of the wind sea by swell [García-Nava *et al.*, 2009]. Whether or not the swell dampens the wind sea in following and cross swell conditions is still a matter of study, as it is the physical mechanism involved.

[54] Besides the attenuation of wind waves by swell described here, Hwang *et al.* [2011b] found that the presence of swell and wind unsteadiness caused an increase of the dimensionless wave variance,  $E_* = E_{ws} g^2 u_*^{-4}$ , during the INTOA experiment. This is explained by the fact that damping of the wind waves not only reduces its energy, but also decreases wind stress. Since  $E_* \propto u_*^{-4}$ , a decrease of  $u_*$  causes an increase of  $E_*$ .

[55] In Figure 10 we present  $E_*$  as a function of dimensionless fetch for the observations made during the INTOA experiment (circles) and those expected in the absence of swell (diamonds and solid line). The diamonds correspond to  $E_*$  calculated with the wave variance computed from the

integration of the frequency spectra reconstructed resembling pure wind sea conditions and the  $u_*$  estimated through the quasi-linear theory using those spectra. For reference we also show the empirical growth functions obtained from the BHDDDB data ensemble with  $u_*$  computed with the similarity functions of the drag coefficient for mixed seas (dashed line) and for pure wind seas (solid line) [Hwang *et al.*, 2011a]. As it can be seen the presence of swell increases the dimensionless wave variance, despite the fact that swell dampens wind sea. The physical meaning is that wave development is more efficient in mixed seas, although the total momentum

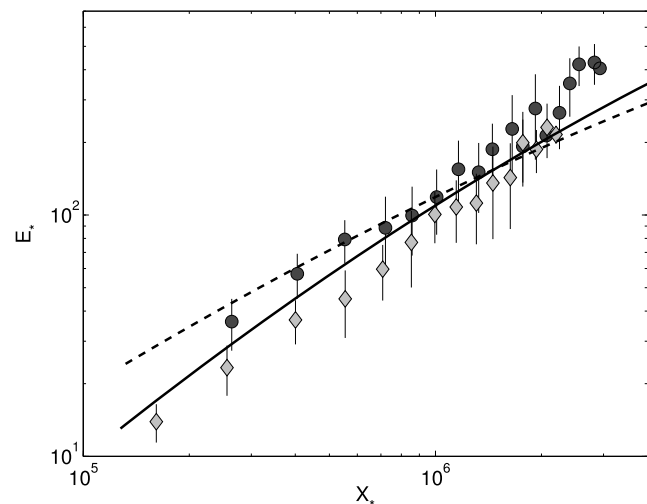


**Figure 10.** Dimensionless wave variance  $E_*$  as a function of dimensionless fetch  $X_*$ . The circles and the diamonds are bin-averaged for data observed during the INTOA experiment, and data representative of wave growth in the absence of swell, respectively. Error bars are two standard deviations. Lines are the empirical growth functions obtained from the BHDDDB data ensemble with  $u_*$  computed with the similarity functions of the drag coefficient for mixed seas (dashed line) and for pure wind seas (solid line) [Hwang *et al.*, 2011a].

transfer from the atmosphere to the ocean is reduced [Hwang *et al.*, 2011b].

[56] As hypothesized by Hwang *et al.* [2011b], a possible explanation for the observed wave development enhancement is that the premature breaking of short waves reduces the momentum transfer from wind to those wave components and allows more of the available wind momentum to be directed to continuous growth of the longer waves. Furthermore, premature breaking leads to an earlier saturation of short waves causing their attenuation, which in turns reduces wave stress and hence total wind stress.

[57] Phillips and Banner [1974] suggested that long waves moving across the surface increase the wind drift near their crests and that the acceleration can be of such magnitude that the maximum particle speed of the short wind waves exceeds their phase speeds causing enhanced wave breaking.

[58] However, a detailed study of the effect of such mechanism, or any others under the action of low steepness opposing swell is beyond the scope of the present work and is being considered as a next step.

[59] A few detailed field observations of developing wind seas in the presence of opposing swell have been reported already. Violante-Carvalho *et al.* [2004] found a small reduction in wave energy in the presence of swell, although they concluded that swell has no significant impact on wind sea growth. Similar conclusions were drawn by Dobson *et al.* [1989], Ardhuin *et al.* [2007], and more recently by Hwang *et al.* [2011b].

[60] In particular, Hwang *et al.* [2011b] found that wave development in opposing swell conditions roughly conforms to the ideal fetch-limited growth functions, even though they found that the presence of swell and wind unsteadiness can cause an enhanced wave development. Equivalently, in Figure 1 it can be seen that, despite the attenuation of wind waves by swell described here, the INTOA wave measurements are in good agreement with the more ideal fetch-limited wave growth functions derived for mixed seas from the BHDDB data ensemble [Hwang *et al.*, 2011b].

[61] These results suggest that the presence of swell and wind unsteadiness can be responsible for some of the scatter observed on wave growth studies but their effect is less significant as compared with the relevance of other phenomena, such as slanting fetch e.g. Ardhuin *et al.* [2007], or atmospheric stability e.g. Kahma and Calhoun [1996] and further show the robustness of fetch-limited growth functions to estimate wave growth under complex conditions.

[62] Finally, as pointed out by one of the reviewers, the swell steepness is a governing parameter for the impact of swell on shorter waves and atmospheric boundary layer [see, e.g. Kudryavtsev and Makin, 2004; Pan *et al.*, 2005; Makin *et al.*, 2007]. In the INTOA data, as the swell steepness increases the response of wind sea significant wave height to wind-forcing is reduced [see Ocampo-Torres *et al.*, 2011, Figure 9], corresponding to a decrease of the wind sea energy with increasing swell steepness. However, the range of variation of swell steepness within the measuring period is rather small for unequivocally assessing this impact of swell. Furthermore, the swell index gives an idea of the relative importance of the swell impact as compared with the wind-forcing, implicitly expressed through the dependence of  $E_w$  on  $u^*$ , and therefore in this study it is preferred over the steepness to characterize the swell influence.

[63] **Acknowledgments.** Suggestions and comments from anonymous reviewers greatly enriched this work. We gratefully acknowledge support by CONACYT (projects: REDESClim, CONACYT 62520, CONACYT-SEP 85108, and SEP-2003-C02-44718) and the Office of Naval Research (Naval Research Laboratory Program Element 61153 N). H.G.N. gratefully acknowledges financial support from DOF-CICESE.

## References

- Anctil, F., M. A. Donelan, W. M. Drennan, and H. C. Graber (1994), Eddy-correlation measurements of air-sea fluxes from a discus buoy, *J. Atmos. Oceanic Technol.*, *11*, 1144–1150.
- Ardhuin, F., T. H. C. Herbers, G. P. van Vledder, K. P. Watts, R. Jensen, and H. C. Graber (2007), Swell and slanting-fetch effects on wind wave growth, *J. Phys. Oceanogr.*, *37*, 908–931, doi:10.1175/JPO3039.1.
- Babanin, M. L., and Y. P. Soloviev (1998), Field investigation of transformation of the wind wave frequency spectrum with fetch and stage of development, *J. Phys. Oceanogr.*, *28*, 563–576.
- Banner, M. L. (1990), Equilibrium spectra of wind waves, *J. Phys. Oceanogr.*, *20*, 966–984.
- Burling, R. W. (1959), The spectrum of waves at short fetches, *Ocean Dyn.*, *12*(2), 45–64.
- Dobson, F., W. Perrie, and B. Toulany (1989), On the deep-water fetch laws for wind-generated surface gravity waves, *Atmos. Ocean*, *27*(1), 210–236.
- Donelan, M. A. (1990), Air-sea interaction, in *The Sea, Ocean Eng. Sci.*, vol. 9, edited by B. LeMehaute and D. M. Hanes, pp. 239–292, John Wiley, Hoboken, N. J.
- Donelan, M. A., and F. W. Dobson (2001), The influence of swell on the drag, in *Wind Stress Over the Ocean*, edited by I. S. F. Jones and Y. Toba, pp. 181–190, Cambridge Univ. Press, New York.
- Donelan, M. A., J. Hamilton, and W. H. Hui (1985), Directional spectra of wind generated waves, *Philos. Trans. R. Soc. London Ser. A*, *315*, 509–562.
- Donelan, M. A., W. M. Drennan, and A. K. Magnusson (1996), Nonstationary analysis of the directional properties of propagating waves, *J. Phys. Oceanogr.*, *26*, 1901–1914.
- Donelan, M. A., W. M. Drennan, and K. B. Katsaros (1997), The air-sea momentum flux in conditions of wind sea and swell, *J. Phys. Oceanogr.*, *27*, 2087–2099.
- Drennan, W. M., M. A. Donelan, N. Madsen, K. B. Katsaros, E. A. Terray, and C. N. Flagg (1994), Directional wave spectra from a swath ship at sea, *J. Atmos. Oceanic Technol.*, *11*, 1109–1116.
- Drennan, W. M., K. K. Kahma, and M. A. Donelan (1999), On momentum flux and velocity spectra over waves, *Boundary Layer Meteorol.*, *92*, 489–513.
- Drennan, W. M., H. C. Graber, D. Hauser, and C. Quentin (2003), On the wave age dependence of wind stress over pure wind seas, *J. Geophys. Res.*, *108*(C3), 8062, doi:10.1029/2000JC000715.
- Fabrikant, A. L. (1976), Quasilinear theory of wind-wave generation, *Izv. Atmos. Ocean. Phys.*, *12*, 524–526.
- García-Nava, H., F. J. Ocampo-Torres, P. Osuna, and M. A. Donelan (2009), Wind stress in the presence of swell under moderate to strong wind conditions, *J. Geophys. Res.*, *114*, C12008, doi:10.1029/2009JC005389.
- Grachev, A. A., and C. W. Fairall (2001), Upward momentum transfer in the marine boundary layer, *J. Phys. Oceanogr.*, *31*(7), 1698–1711.
- Hasselmann, K., et al. (1973), Measurements of wind-wave growth and swell decay during the Joint North Sea Wave Project (JONSWAP), *Ergänzungsh. Deutsch. Hydrogr. Zeitschr.*, *A*(8<sup>o</sup>)(12), 1–95.
- Hwang, P. A. (2008), Observation of swell influence on ocean surface roughness, *J. Geophys. Res.*, *113*, C12024, doi:10.1029/2008JC005075.
- Hwang, P. A., and D. W. Wang (2004a), An empirical investigation of the source term balance of small scale surface waves, *Geophys. Res. Lett.*, *31*, L15301, doi:10.1029/2004GL020080.
- Hwang, P. A., and D. W. Wang (2004b), Field measurements of duration-limited growth of wind-generated ocean surface waves at young stage of development, *J. Phys. Oceanogr.*, *34*, 2316–2326.
- Hwang, P. A., H. García-Nava, and F. J. Ocampo-Torres (2011a), Dimensionally consistent similarity relation of ocean surface friction coefficient in mixed seas, *J. Phys. Oceanogr.*, *41*, 1227–1238, doi:10.1175/2011JPO4566.1.
- Hwang, P. A., H. García-Nava, and F. J. Ocampo-Torres (2011b), Observations of wind wave development in mixed seas and unsteady wind forcing, *J. Phys. Oceanogr.*, *41*, 2340–2359, doi:10.1175/2011JPO-D-11-044.1.
- Janssen, P. A. E. M. (1989), Wave-induced stress and the drag of air flow over sea waves, *J. Phys. Oceanogr.*, *19*, 745–754.
- Janssen, P. A. E. M. (1991), Quasi-linear theory of wind-wave generation applied to wave forecasting, *J. Phys. Oceanogr.*, *21*, 1631–1642.

- Janssen, P. A. E. M. (2004), *The Interaction of Ocean Waves and Wind*, 300 pp., Cambridge Univ. Press, Cambridge, U. K.
- Janssen, P. A. E. M., P. Lionello, and L. Zambresky (1989), On the interaction of wind and waves, *Philos. Trans. R. Soc. London A*, *329*, 289–301.
- Kahma, K. K., and C. J. Calhoun (1996), Growth curve observations, in *Dynamics and Modelling of Ocean Waves*, edited by G. J. Komen et al., pp. 174–182, Cambridge Univ. Press, New York.
- Komen, G. J., L. Cavaleri, M. A. Donelan, K. Hasselmann, S. Hasselmann, and P. A. E. M. Janssen (Eds.) (1996), *Dynamics and Modelling of Ocean Waves*, 532 pp., Cambridge Univ. Press, New York.
- Kudryavtsev, V. N., and V. K. Makin (2004), Impact of swell on the marine atmospheric boundary-layer, *J. Phys. Oceanogr.*, *34*, 934–949.
- Long, C. E., and D. T. Resio (2007), Wind wave spectral observations in Currituck Sound, North Carolina, *J. Geophys. Res.*, *112*, C05001, doi:10.1029/2006JC003835.
- Longuet-Higgins, M., D. E. Cartwright, and N. D. Smith (1963), Observations of the directional spectrum of sea waves using motions of a floating buoy, in *Ocean Wave Spectra*, pp. 111–136, Prentice Hall, Upper Saddle River, N. J.
- Makin, V. K., and V. N. Kudryavtsev (1999), Coupled sea surface-atmosphere model, 1. wind over waves coupling, *J. Geophys. Res.*, *104*(C4), 7613–7623.
- Makin, V. K., H. Branger, W. L. Pierson, and J. P. Giovanangeli (2007), Stress above wind-plus-paddle waves: Modelling of a laboratory experiment, *J. Phys. Oceanogr.*, *37*, 2824–2837, doi:10.1175/2007JPO3550.1.
- Ocampo-Torres, F. J., H. García-Nava, R. Durazo, P. Osuna, G. M. Díaz Méndez, and H. C. Graber (2011), The INTOA experiment: A study of ocean-atmosphere interactions under moderate to strong offshore winds and opposing swell conditions in the Gulf of Tehuantepec, México, *Boundary Layer Meteorol.*, *138*, 433–451, doi:10.1007/s10546-010-9561-5.
- Pan, J., D. W. Wang, and P. A. Hwang (2005), A study of wave effects on wind stress over the ocean in a fetch-limited case, *J. Geophys. Res.*, *110*, C02020, doi:10.1029/2003JC002258.
- Phillips, O. M. (1985), Spectral and statistical properties of the equilibrium range in wind-generated gravity waves, *J. Fluid Mech.*, *156*, 505–531.
- Phillips, O. M., and M. L. Banner (1974), Wave breaking in the presence of wind drift and swell, *J. Fluid Mech.*, *66*, 625–640.
- Resio, D. T., C. E. Long, and C. L. Vincent (2004), Equilibrium-range constant in wind-generated wave spectra, *J. Geophys. Res.*, *109*, C01018, doi:10.1029/2003JC001788.
- Romero, L., and W. K. Melville (2010), Airborne observations of fetch-limited waves in the Gulf of Tehuantepec, *J. Phys. Oceanogr.*, *40*, 441–465, doi:10.1175/2009JPO4127.1.
- Romero-Centeno, R., J. Zavala, A. Gallegos, and J. J. O'Brien (2003), Isthmus of Tehuantepec wind climatology and ENSO signal, *J. Clim.*, *16*, 2,628–2,639.
- Violante-Carvalho, N., F. J. Ocampo-Torres, and I. Robinson (2004), Buoy observations of the influence of swell on wind waves in the open ocean, *Appl. Ocean Res.*, *26*, 49–60.
- WAMDI (1988), The WAM model—A third generation ocean wave prediction model, *J. Phys. Oceanogr.*, *18*, 1775–1810.